Research Article

# Extraordinary impact resistance of carbon nanotube film with crosslinks under micro-ballistic impact

Kailu Xiao [a, b, 1], Xudong Lei [a, b], Yuyu Chen [a, b], Qi An [c, d], Dongmei Hu [e, 1], Chao Wang [a, **], Xianqian Wu [a, *], Chenguang Huang [a, b]

[a] Institute of Mechanics, Chinese Academy of Sciences, Beijing, 100190, China
[b] School of Engineering Science, University of Chinese Academy of Sciences, Beijing, 100049, China
[c] Department of Chemical and Materials Engineering, University of Nevada, Reno, NV, 89557, USA
[d] Nevada Institute for Sustainability, University of Nevada, Reno, NV, 89557, USA
[e] Key Laboratory of Multifunctional and Smart Systems, Suzhou Institute of Nano-Tech and Nano-Bionics, Chinese Academy of Sciences, Suzhou, 215123, China

## ARTICLE INFO

## ABSTRACT

The crosslinks of carbon nanotubes (CNT) film has been demonstrated to owing the ability to reinforce the quasi-static mechanical properties. But it is unclear whether crosslinks improve the ballistic impact resistance of CNT film. Here, we investigated the impact resistance of CNT film with crosslinks by combining micro-ballistic impact experiments with coarse-grained molecular dynamics (CGMD) simulations. The impact resistance is quantitatively characterized in terms of the specific penetration energy. Meanwhile, the effective enhancement of impact resistance contributed to the crosslinks is directly observed in the experiment. CGMD simulations are employed to unveil the corresponding mechanisms in terms of deformation behavior, energy dissipation mode, and failure behavior. Our results indicate that with the increase of crosslink density, the energy dissipation mode of the CNT film transforms from bending-dominated to stretching-bending-dominated due to enhanced interaction between the adjacent CNTs. This leads to a transformation of perforated morphology from cascaded interfaces sliding to crosslink-restricted deformation with crosslinks. Our simulations also indicate that the length, bending stiffness of CNTs, and film's thickness play essential roles in the impact resistance of CNT film at various crosslink densities. These results provide a feasible strategy to improve the protective performance of CNT film.

## 1. Introduction

Advanced materials with light-weight and superior impact resistance are essential for impact engineering of bullet-proof body armor [1,2] and debris-proof spacecraft shielding [3,4]. In recent years, carbon nanotube (CNT) film with nano-network structures has attracted great attention due to its excellent multifunctional properties such as superior flexibility, tunable pore density, and large surface-to-volume and strength-to-weight ratios [5—9]. In addition, the excellent energy dissipation behavior of CNT film

under impact makes it an ideal protective material.

Extensive research has been dedicated to determining the mechanical properties of CNT films under quasi-static loadings, with the emphasis generally focused on the type of CNT and the microstructures. Sakurai et al. [10] investigated the mechanical strength of CNT film comprised of millimeter-length single-walled CNT (SWCNT). The results showed that the strength of the SWCNT film with fiber lengths of 1500 μm was more than twice (45 vs. 19 MPa) that of CNT film with fiber lengths of 350 μm. Ma et al. [11] observed that the Poisson's ratio of CNT film changes from negative to positive during uniaxial tensile loadings due to the variation of angles between CNTs and the elongation of initial-bent CNTs. Cranford et al. [12] numerically tuned Young's modulus of CNT film over a range of 0.2—3.1 GPa by manipulating the type and density of the CNT based on the developed coarse-grained molecular dynamics (CGMD) model. Xie et al. [8] investigated the relationship

between microstructure and mechanical properties of CNT film through CGMD simulations. Their results showed that the mechanical properties of CNT film could be enhanced by inhibiting the inter-tube sliding during the loading process.

Such the mechanical properties of CNT film as Young's modulus and strength do not exhibit performance superior to advanced metals [13,14] and fibers [15,16]. However, recent studies indicate that the CNT film exhibits an excellent capacity for energy dissipation under dynamic loadings due to the disordered and tunable nano-network structures [17], making it great potential to be the next generation of impact protective materials. Wang et al. [18] employed CGMD simulations to reveal that brittle fracture of the CNTs and detachment or sliding-induced ductile failure of vdW interfaces between the CNTs render abundant channels to dissipate impact energy. Another CGMD study by Chen et al. [19] also showed that the CNT film possesses extremely high efficiency to dissipate impact energy within its deformation limits during high-velocity plate-impact.

The aforementioned studies on the dynamic behavior of CNT film indicate that the interactions between CNTs in the film involving bending, sliding, and bundling play a significant role in the energy dissipation process. An intriguing question, therefore, arises: if reinforcing the interaction by introducing crosslinks between adjacent CNTs, can the impact resistance of the CNT film be improved dramatically? It is well known that both physical crosslinks [20,21] and chemical crosslinks [22,23] can significantly improve the mechanical properties of CNT film [17,24–26], e.g. the increase of quasi-static tensile strength by 4–7 times. Regarding the mechanical properties under quasi-static loadings, one could expect a superior impact resistance for the CNT film with crosslinks. However, up to now, no direct experimental evidence or simulation result has yet been reported to prove this fascinating expectation.

In this study, the effects of crosslinks on the micro-ballistic impact resistance of CNT film are investigated by experiments and CGMD simulations. Firstly, micro-ballistic impact experiments showed the improvement of impact resistance of CNT films by introducing crosslinks. Then a series of CGMD simulations are conducted to obtain the specific penetration energy of the CNT films with crosslinks concerning the crosslink density. The superior impact energy dissipation mechanisms of CNT films in terms of dynamical responses, energy dissipation modes, and failure behaviors are investigated by simulations. The failure characteristics involving the change of broken morphology around the penetration hole and the shrinkage effect of the post-mortem penetration hole of CNT film after adding crosslinks are compared qualitatively between experiment and simulation results. The key parameters that affect the energy dissipation ability of the CNT film with crosslinks such as length, bending stiffness of CNT, and thickness of CNT film are also investigated in the simulations. This study provides solid evidence that the impact resistance of CNT film can be enhanced by introducing crosslinks. The strategy is proposed for designing a CNT film with further improved protective performance.

## 2. Experimental method and computational model

### 2.1. Micro-ballistic impact experiments

To explore the impact performance of CNT films with and without crosslinks, a laser-induced micro-particle impact test (LIPIT) platform, which was originally developed by Lee et al. [27] and further improved by Hassani-Gangaraj et al. [28,29], was built as illustrated in Fig. 1(a). In LIPIT experiments, high-pressure plasma under the confinement of a 4-mm-thick BK7 glass is generated through the interaction between the focused pulse-laser (1064 nm wavelength, 10 ns FWHM, Φ2 mm) and a 40-μm-thick

aluminum film, resulting in the rapid swelling of a 100-μm-thick polydimethylsiloxane (PDMS) film attached closely to the aluminum (Al) film. During that process, a steel projectile with a diameter of 360 μm placed at the back surface of the PDMS film is accelerated and then impacts the boundary-fixed CNT films with an average speed of ~100 m/s determined by the high-speed photography (specialised-imaging SIMD16). The residual velocity was also measured to obtain the impact resistance of the CNT film. Both the CNT films in the pristine state (density ~0.42 g/cm$^3$) and the CNT film with polyvinyl alcohol (PVA) as crosslinks (density ~0.53 g/cm$^3$) were tested to investigate the effects of crosslinks. Compared with weak vdW connections between CNT fibers, the crosslink is generally defined as enhanced connections between CNT chains [25], which can be realized by adding a small amount of PVA in experiments that strengthens the weak vdW interfaces. The coarse-grained molecular dynamics (CGMD) simulation aims to investigate the enhancement effect of the crosslinks as observed in experiments implemented by adding extra bonds between CNT chains. It is to be noted that a ceiling of weight and spatial dimensions of CNT film exists for crosslinks constructed in this experiment due to the saturation threshold after soaking and solvent evaporation. The post-mortem fractured films were characterized by Scanning Electron Microscope (SEM) to understand the dynamic deformation and failure behavior.

### 2.2. Coarse-grained models for CNT films

A CGMD model is constructed based on Refs. [30,31] to simulate the realistic CNT systems. Each 100-nm-length CNT chain consists of 100 beads, and a coarse-grained bead is mapped by a (5, 5) SWCNTs with the same mass. The bonding between two adjacent beads and the angle interaction from three successive beads in a certain CNT chain are represented by springs to reflect the stretching and bending properties. The inter-tube interaction between the pairs of beads is depicted by the long-ranged vdW interaction. Therefore, the deformation energy of the coarse-grained system can be calculated by stretching energy of intrinsic bonds $E_s$, stretching energy of extra bonds of crosslinks $E_c$, bending energy $E_b$, and vdW energy $E_v$ as given by

$$E_{total} = E_s + E_c + E_b + E_v, \tag{1a}$$

$$E_s = \sum_{bonds} k_s (r - r_0)^2 / 2, \tag{1b}$$

$$E_c = \sum_{crosslinks} k_s (l - l_0)^2 / 2, \tag{1c}$$

$$E_b = \sum_{angles} k_\varphi (\varphi - \varphi_0)^2 / 2, \tag{1d}$$

$$E_v = \sum_{pairs} 4\varepsilon \left[ (\sigma/r)^{12} - (\sigma/r)^6 \right], \tag{1f}$$

where $k_s$ is stretching stiffness related to the current bond length $r$, and the length in the equilibrium state $r_0$ is 10 Å. $l$ denotes the added bond length, and the length in the equilibrium state $l_0$ is 10 Å. $k_\varphi$ denotes bending stiffness related to the current angle of the triplet $\varphi$, and the angle in the equilibrium state $\varphi_0$ is 180°. $\epsilon$ and $\sigma$ represent the depth of the potential well and zero energy inter-tube distance, respectively. All parameters used in CGMD simulations are calibrated from full-atom MD simulation and depicted in Table 1. The cutoff value applied to non-bonding pair interaction is
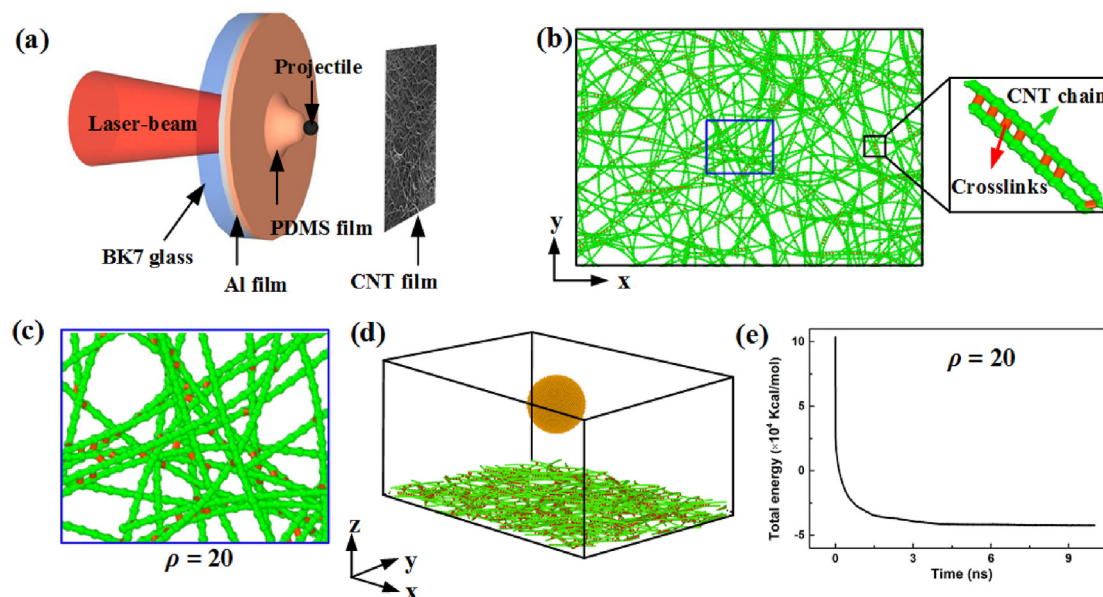
**Fig. 1.** (a) Schematic of laser-induced projectile impact experimental tests. (b) Cross-linked CNT film in simulation with $\rho = 20$ in the top view and the enlarged view represents crosslinks between two nanotubes (CNTs are shown in green and crosslinks are shown in red). (c) Morphology of enlarged CNT film in simulation as marked in (b) by blue rectangle to illustrate the uniform distribution of crosslinks. (d) Micro-projectile impact model in simulation (CNT film is shown in green, and the projectile is illustrated in orange). (e) Total energy for the simulation system during the equilibrium NVT ensemble for $\rho = 20$. (A colour version of this figure can be viewed online.)

**Table 1**
Parameters of the force field for the coarse-grained (5, 5) SWCNT model [12].

| Parameters | $k_s$ | $r_0$ | $k_\varphi$ | $\varphi_0$ | $\sigma$ | $\epsilon$ |
|---|---|---|---|---|---|---|
| Value | 1000 | 10 | 14300 | 180° | 9.35 | 15.1 |
| Units | kcal/mol/Å² | Å | kcal/mol/rad² | – | Å | kcal/mol |

4 nm. The bond breaks once the tensile strain exceeds 24%, which has been verified in the previous study [18]. Pairs of beads within distance 0.8−1.2 nm are chosen by a detection program and then selected randomly to generate crosslinks. Without loss of generality, the inter-tube crosslinks adopted here are assumed to be the same as the intra-tube bonds.

To simulate the experimental system as well as possible, we constructed the coarse-grained numerical model according to the geometry scaling relation [32] as listed in Table 2, where *L*, *t*, and *D* denote the length of an individual CNT chain, the thickness of the CNT film and the diameter of projectile, respectively. It can be seen that the dimensionless in-plane size $\eta = L/D$ and the dimensionless thickness $\chi = t/D$ in our simulation are almost in the same order as that in the experiments, implying the same deformation mechanisms between the experiments and the simulations.

It should be noted that we study the enhancement effect of PVA by adding some bonds between adjacent CNTs, and additional PVA beads are not introduced in the numerical model. The rationality of this treatment is based on the following experimental evidences: firstly, the length of the PVA chain is much smaller than that of CNTs, ~0.15 μm vs. ~300 μm; secondly, the volume fraction of PVA is relatively small, ~6.8%, and the CNT film can still be viewed as a porous material. Therefore, it is appropriate to adopt the bond model in our simulation to simulate the enhanced connections between neighbor CNTs by PVA and ignore the volume effect of PVA molecules. This crosslink strategy not only captures the enhanced effect of crosslinks by PVA, but also effectively improves computational efficiency. Moreover, this scheme has been successfully adopted to study the effect of crosslinks on the mechanical deformations [8,33], viscoelastic properties [34], and fracture behaviors [35] of CNT films.

### 2.3. Micro-ballistic impact model

All CGMD simulations are performed by adopting the large-scale atomic/molecular massively parallel simulator (LAMMPS) [36] and the results are visualized in the Open Visualization Tool (Ovito) software [37]. Fig. 1(b) shows the CNT film with crosslinks, in which the CNT chains and crosslinks are pointed and color-coded by green and red, respectively. The crosslinks' density, $\rho$, is defined as the average number of crosslinks per coarse-grained CNT chain [35]. The crosslinks are distributed uniformly in the CNT film as shown in Fig. 1(c) for the system with $\rho = 20$. The maximum crosslink density, which is caused by the limitation of adjacent beads distance, is determined as $\rho_{max} = 35$ in the simulation configuration, the value of which is consistent with the ceiling we observed experimentally. The density of the CNT film at the equilibrium state is 0.28 g/cm³, which is comparable with the magnitude of density adopted in the experiments.

After the CNT films with crosslinks are prepared, a spherical diamond projectile with a diameter of 20 nm is constructed and added to the system as shown in Fig. 1(d). The initial distance between projectile and CNT film is about 10 nm to avoid the interaction during the relaxation stage. Here, the projectile is considered as a rigid body since the projectile is much stronger than CNT film and no broken of the projectile is observed in experiments. The CNT film is periodic-boundary conditions along with the non-impact directions, i.e. X−Y directions, and free-standing in the impact direction, i.e. Z direction. About 2 nm are set as fixed-boundary at the

**Table 2**
Dimensions of experiments and CGMD simulations.

| Methods | *L* | *t* | *D* | $\eta = L/D$ | $\chi = t/D$ |
|---|---|---|---|---|---|
| Experiments | 300−360 μm | 10 μm | 360 μm | 1.2−1 | 0.03 |
| CGMD simulations | 20−100 nm | 4−5 nm | 20 nm | 1−5 | 0.2−0.25 |

peripheries along X and Y direction during the impact process. The interaction between the CNT film and the projectile is considered as 12-6 Lennard-Jones potential described by Eq. (1d), and the parameters are the same as the inter-tube interactions. The whole system is equilibrated at 300 K for 10 ns using the NVT ensemble with a Langevin thermostat. The total energy fluctuation is less than 0.1% after equilibrium as given in Fig. 1(e). After that, the canonical ensemble (i.e. NVE) is adopted for the impact tests, and a time step of 1 fs is applied to ensure the stability of the simulation. A series of impact tests from non-perforation to perforation are conducted with impact velocities, $v_i$, ranging from 8 to 12 km/s.

## 3. Results and discussion

### 3.1. Experimental results

To examine the dynamical responses of CNT film with crosslinks, the LIPIT tests on CNT film without and with crosslinks were performed. The energy change of the projectile before and after impact, $\Delta E_k$, equals the absorption energy of the membrane during the impact process, $E_p$. The energy loss of air drag can be ignored. Here, $\Delta E_k = m(v_i^2 - v_r^2)/2$ and $E_p = (\rho A_s t)v_i^2/2 + E_d$, where the first term of the latter equation represents the kinetic energy transfer from the projectile to the film within the deformation area $A_s$. $m$ denotes the mass of the projectile, $v_i$ and $v_r$ represent the impact velocity and residual velocity of the projectile, $t$ is the thickness of the film. $E_d$ is the other possible energy dissipation channels like propagation of cracks. The specific penetration energy, $E_p^*$, is defined as the normalized absorption energy of CNT films by the mass of film within the impact region, and it is adopted to evaluate the energy dissipation ability of CNT film [27]. The specific penetration energy can be written as $E_p^* = E_p/\rho A_s h = v_i^2/2 + E_d^*$, where $\rho$ denotes the density of the film, and $E_d^*$ is the delocalized penetration energy served to evaluate the outward propagation ability of stress wave and is material-dependent.

The $E_p$ of CNT films with and without crosslinks are about $5.5 \times 10^{-4}$ J and $4.1 \times 10^{-4}$ J, respectively, under $v_i = 100$ m/s, implying that the crosslinks can effectively enhance the energy absorption capability (i.e. 34% improvement after adding crosslinks) and improve the ballistic resistance of CNT film. Corresponding, the $E_p^*$ of CNT films with and without crosslinks are determined to be 0.81 MJ/kg and 1.0 MJ/kg, respectively, which are much higher than other bulletproof materials such as Al (0.12 MJ/kg) [38], steel (0.1 MJ/kg) [39], Kevlar armor (0.5 MJ/kg) [40], and PMMA (0.12 MJ/kg) [41]. This phenomenon indicates the great potential of CNT film as an advanced bulletproof material. It is worth noting that $E_p^*$ of CNT film with crosslinks is slightly lower than the pristine CNT film due to the extra mass of the PVA adhesion, i.e. 27% weight increment after adding crosslinks. Because no extra mass is introduced, one could expect extremely higher $E_p$ and $E_p^*$ of CNT film with crosslinks introduced by other methods such as e-beam irradiation [22] instead of polymer adhesions.

After the micro-ballistic impact tests, the post-mortem fractured morphologies for the CNT films with and without crosslinks were examined as given in Fig. 2(a) and (b), respectively. The cascaded interface sliding mode is observed for CNT film without crosslinks, in which abundant CNT fibers on the periphery of the penetration hole are pulled out after impact due to the weak vdW interfaces between CNT chains, leading to a fluffy microstructure as marked in Fig. 2(a). In contrast, a much smooth profile as illustrated in Fig. 2(b) is formed for the CNT film with crosslinks due to the PVA crosslinks between the adjacent CNT chains that strongly restrict the sliding behavior of the CNT chains. The interesting transformation of damage mode from the cascaded interface sliding to the crosslink-restricted deformation after adding crosslinks implies the mechanism change of energy dissipation, which contributes to the improvement of the impact resistance of the CNT film with crosslinks. Therefore, a series of CGMD simulations need to be conducted to thoroughly investigate the effects of crosslinks and the corresponding microscopic energy dissipation mechanism qualitatively.

### 3.2. Crosslink-density-dependent protective performance

To further understand the effect of crosslinks and elucidate this transition of damage mode, the CGMD simulations were performed. The residual velocity, $v_r$, of the projectile and the specific penetration energy, $E_p^*$, of the CNT film with respect to the crosslink density are given in Fig. 3. As shown in Fig. 3(a), for $v_i = 12$ km/s, all the CNT films with even the largest crosslink density $\rho = 35$ are perforated as indicated by the inserted microstructure, and $v_r$ decreases almost linearly with the increase of $\rho$. Correspondingly, the $E_p^*$ increases almost linearly from 88 MJ/kg to 102.5 MJ/kg at $v_i = 12$ km/s, namely an increase of 16.5% as we increase the crosslink density $\rho$ from 0 to 35. While decreasing the impact velocity to $v_i = 8$ km/s, only the CNT films with the crosslink density $\rho \leq 20$ are perforated as given by the inserted microstructures. For $\rho \leq 10$, $v_r$ decreases nearly linearly with $\rho$, and the slope is approximately same as $v_i = 12$ km/s, leading to the linear increase of $E_p^*$ from 34.2 MJ/kg to 37.4 MJ/kg with respect to $\rho$ as depicted in Fig. 3(b). The CNT film is perforated by the projectile for $\rho \leq 20$. For
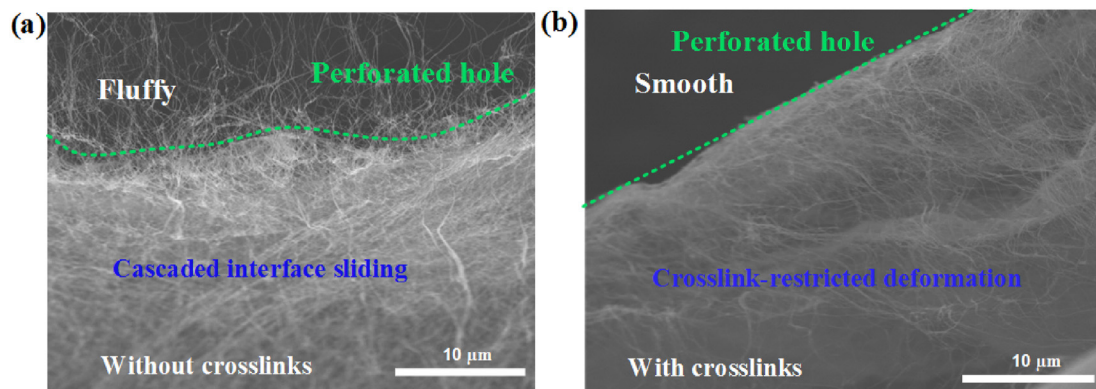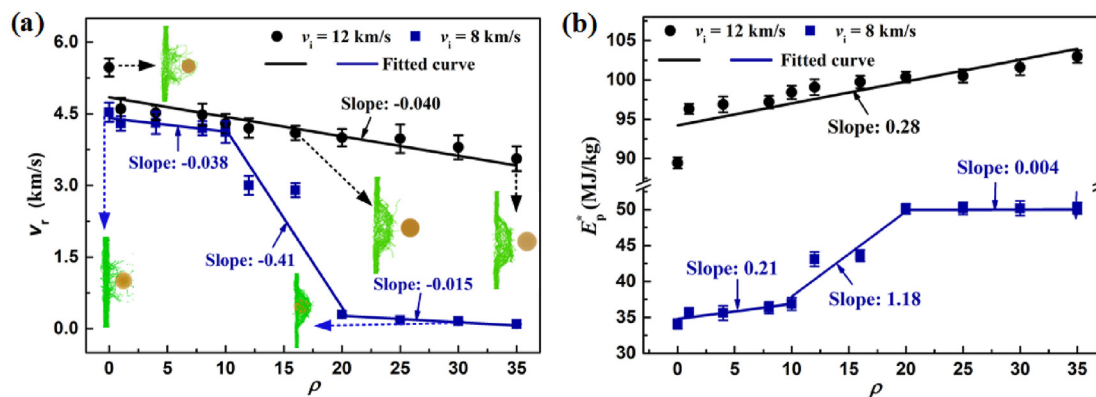


**Fig. 2.** SEM images of the broken morphologies for (a) the pristine CNT film and (b) the CNT film with crosslinks, respectively. (A colour version of this figure can be viewed online.)

**Fig. 3.** (a) Residual projectile velocities and (b) the specific penetration energy of the CNT films with increased crosslink densities $\rho$ at $v_i = 12$ km/s and 8 km/s obtained from the CGMD simulations. (A colour version of this figure can be viewed online.)

$\rho > 20$, $v_r$ and $E_p^*$ almost remain constant with respect to $\rho$ because the CNT films are not perforated. All the phenomena could be observed in movies in Supplementary Materials. Since $v_i = 8$ km/s is almost the critical impact velocity $v_c$ [42] for $\rho = 20$, $v_r$ decreases fast to almost 0 m/s for $10 < \rho \leq 20$. Correspondingly, $E_p^*$ rapid increases to 50 MJ/kg as $\rho$ increases to 20. The corresponding deformation mechanism for perforation to non-perforation is much different as well. For the case of perforation, it is the local tensile failure of the film near the impact region that dissipates the impact energy. However, for the case of non-perforation, the stretching and bending of almost the whole CNT film contribute to the dissipation of the impact energy. This enhancement after adding crosslinks is consistent with the experiments that the energy absorption capacity has been improved after adding PVA. The specific penetration energy in the simulations is nearly two orders of magnitude larger than that in the experimental results, which is ascribed to the different sizes of CNT films as adopted in experiments and simulations. Both the high specific impact kinetic energy $v_i^2/2$ and delocalized penetration energy $E_d^*$ at high impact velocity contribute to the high $E_p^*$ in the simulations. The delocalized penetration energy $E_d^*$ of the CNT films without crosslinks is estimated to be 3 and 18 MJ/kg at 8 and 12 km/s, respectively, based on the simulation. In addition, $E_d^*$ increases to about 30.5 MJ/kg in simulation while increasing the crosslink density to $\rho = 35$ at $v_i = 12$ km/s. It is, therefore, reasonable to believe that more energy dissipation channels could be triggered at high impact velocity and crosslink density, which will be discussed in the next sections.

### 3.3. Deformation behavior of CNT films

As illustrated by experiments, the impact-induced deformation mode of CNT films changes after adding crosslinks. To better understand the strengthening mechanism of crosslinks, the morphology evolutions of in-plane fracture of the CNT films with $\rho = 0$ and 20 at $v_i = 12$ km/s were analyzed and shown in Fig. 4. At 5 ps, the perforation occurs with a perforated hole as marked by the dashed blue circles accompanying with some broken bonds as marked in red. The microstructure evolutions for $\rho = 0$ and 20 are different. For $\rho = 0$, the perforated hole with fluffy-edge is formed due to the cascaded interface sliding as shown in Fig. 4(a). As the density of crosslinks increases to 20, however, the perforated hole with smooth edges is observed due to the strong interactions between adjacent CNT chains that suppress the interfacial sliding of CNT fibers as given in Fig. 4(b). The damage morphologies obtained

from simulations agree very well with the experimental observation as depicted in the insets of Fig. 4 at 5 ps. Furthermore, the perforated hole of the CNT film without crosslink, i.e. $\rho = 0$, expands continually after impact from 10 to 20 ps. In contrast, it begins to shrink with the addition of crosslinks (e.g. $\rho = 20$) after impact due to the recovery of elastic deformation, as shown in Fig. 4. This shrinkage effect is also observed in experimental results by measuring the size of the post-mortem penetration hole in the insets of Fig. 4 at 20 ps. Experimentally, for the CNT film without PVA, the size of the penetration hole is ~510 μm, which is much larger than the projectile diameter (~360 μm). It decreases to ~300 μm after adding PVA and is smaller than the projectile diameter. This "shrink" of the penetration hole with crosslinks can be well understood by the constrained sliding effects of the CNT chains introduced by the PVA, making the deformation of the CNT films around the penetration hole recover partially after penetration. Besides, the number of broken bonds, $N_b$, increases from 56 to 73 with the increase of $\rho$ from 0 to 20, indicating a transformation of damage mode from vdW interfaces sliding to covalent bonds breaking of intra-chains.

As depicted in Fig. 5(a), the out-of-plane displacement, $z$, the diameter of conic deformation, $d_c$, and the diameter of the perforated hole, $d_b$, are extracted to quantitatively describe the influence of crosslinks on the dynamical responses of the CNT films at $v_i = 12$ km/s. Fig. 5(b) indicates that the out-of-plane displacement increases linearly with time for $\rho = 0$ after the perforation occurs at 5 ps due to the inertial effects. With the increase of $\rho$, the out-of-plane displacement after impact decreases quickly, implying that the added bonds can effectively restrict the sliding of CNT chains and further increase the out-of-plane bending stiffness of the CNT films. The snapshots of structure morphologies as shown in the inset of Fig. 5(b) also clearly characterize the less deformation localization of the CNT film with $\rho = 20$ compared to $\rho = 0$. As shown in Fig. 5(c), during the expansion of the conic deformation, the diameter of the conic region, $d_c$, increases with the crosslink density $\rho$ and provides more area to dissipate the impact energy, indicating a faster conic velocity at a larger $\rho$. A relatively larger basal diameter yet a smaller out-of-plane displacement is observed after adding crosslinks. The diameter of the perforated hole, $d_b$, of the CNT film has the largest value for $\rho = 0$ and increases linearly with time throughout the observation duration as shown in Fig. 5(d). However, when the crosslink density, $\rho$, increases to 10 and 20, $d_b$ is smaller than that in $\rho = 0$ and tends to decrease after penetration, indicating the transformation from continued sliding to partial recovering after adding crosslinks. Therefore, crosslinks
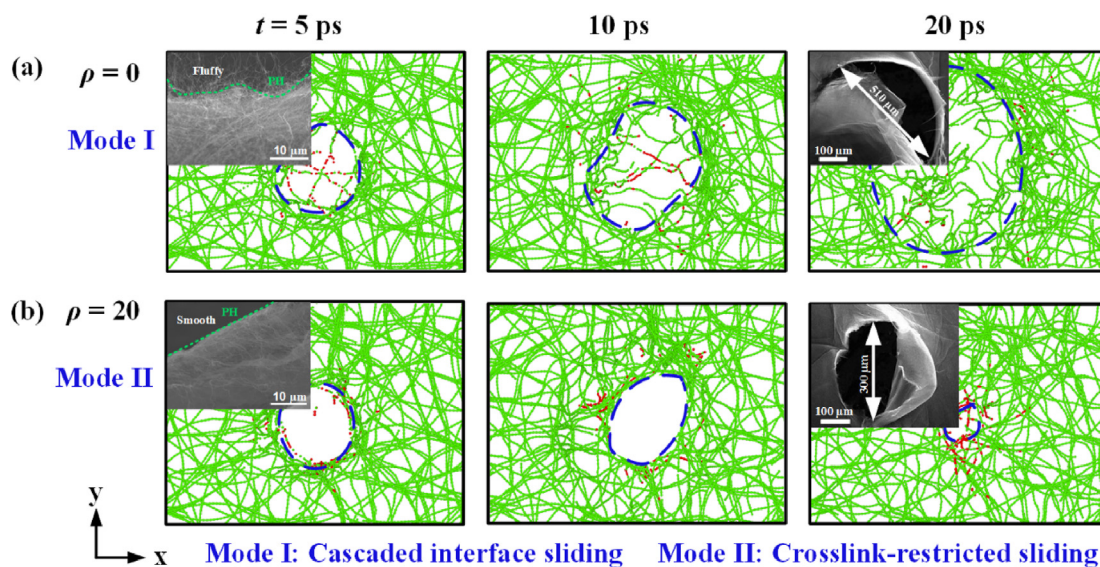
**Fig. 4.** Perforated morphologies of CNT films for (a) $\rho = 0$ and (b) $\rho = 20$, respectively, at $v_i = 12$ km/s from simulations, which match well with the experiments result as given in the insets. The marked red beads represent the broken bonds caused by the impact event. (A colour version of this figure can be viewed online.)
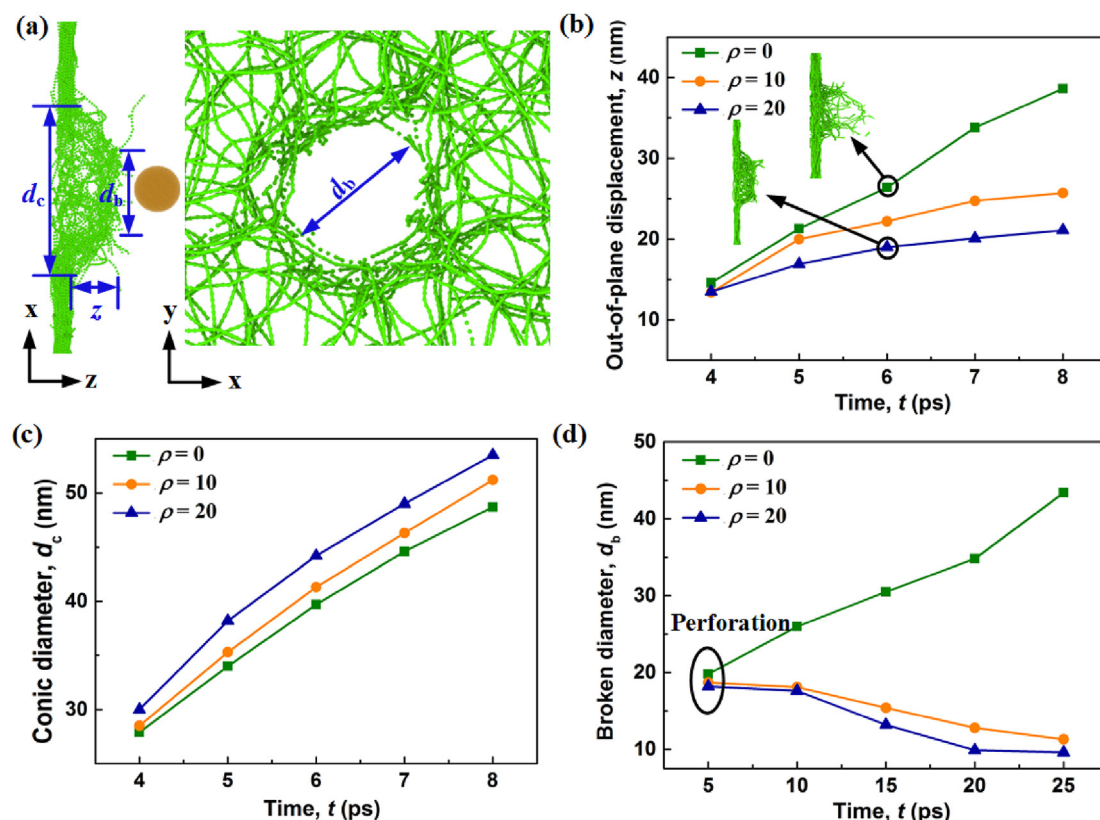


**Fig. 5.** Simulated deformation behavior of CNT films. (a) Schematic of deformation behavior. (b), (c) and (d) Histories of out-of-plane displacement, diameter of conic deformation, and diameter of penetration hole for $\rho = 0$, 10, and 20, respectively. (A colour version of this figure can be viewed online.)

among the CNTs dramatically increase the interaction between the tubes and significantly strengthen the weak interfaces. The increase of the difference between $d_c$ and $d_b$, $d_c - d_b$, indicates more deformation delocalization with the increased density of crosslink and therefore more area participated in dissipating the impact energy, resulting in a relatively high specific penetration energy.

### 3.4. Energy dissipation mode and failure mechanisms

It is vital to reveal the energy dissipation mode and failure mechanisms of CNT films with various crosslink densities by numerical simulations to help design high-performance CNT films experimentally. The change of potential energy, $\Delta E$, can correspondingly be decomposed into the change of bending energy $\Delta E_b$,
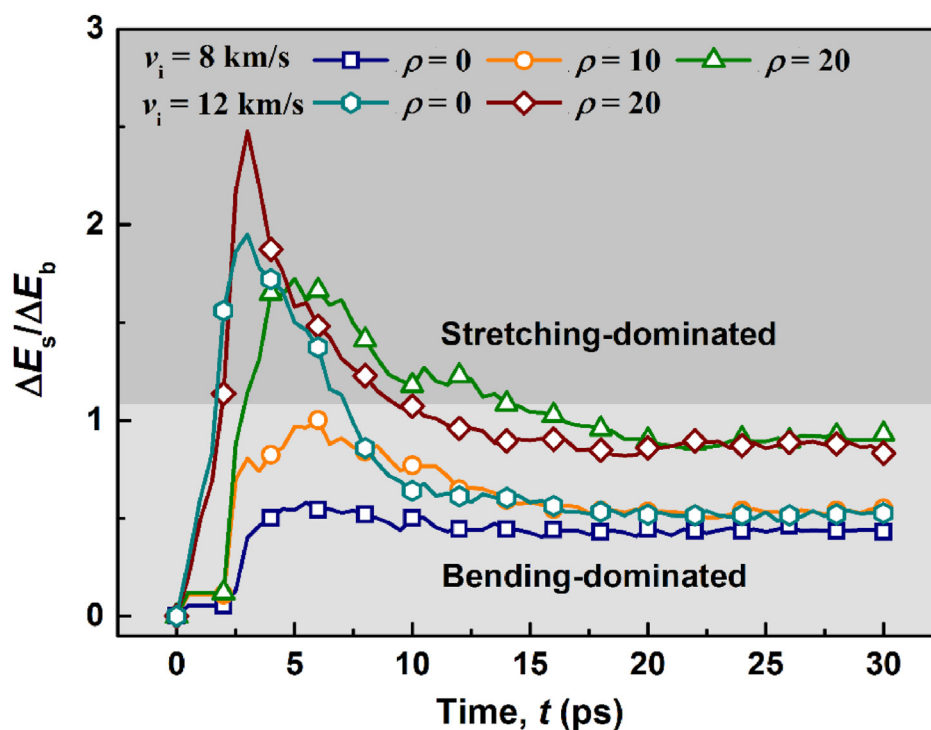
**Fig. 6.** Histories of $\Delta E_s/\Delta E_b$ of the CNT films with various crosslink densities at $v_i$ = 8 km/s and 12 km/s based on CGMD simulation results. (A colour version of this figure can be viewed online.)

stretching energy $\Delta E_s$, and vdW energy $\Delta E_v$. Here, the ratio of the $\Delta E_s$ to the $\Delta E_b$, i.e. $\Delta E_s/\Delta E_b$, is used to explore the major energy dissipation mode [35,43]. For $v_i$ = 8 km/s, $\Delta E_s/\Delta E_b$ is smaller than 1 for $\rho$ = 0 and 10 during the whole impact process as depicted in Fig. 6, indicating the energy dissipation mode is dominated by the bending of CNT fibers, which is consistent with a previous study by Wang et al. [18]. For $\rho$ = 20, $\Delta E_s/\Delta E_b$ initially increases quickly and exceeds 1 after 2.5 ps, and then reaches the maximum value at 5 ps when the perforation occurs. After that, it decreases constantly and becomes smaller than 1, indicating the stretching-bending two-stage dominant energy dissipation mode for the CNT films with a larger crosslink density. A critical crosslinks density, $\rho_c$ = 10, for transformation from the one-stage bending to the two-stage stretching-bending dominant mode, is observed under $v_i$ = 8 km/s. Once the stretching-bending-dominated energy dissipation is triggered after adding crosslinks, there are more additional channels to dissipate the impact energy and therefore enhance the specific penetration energy $E_p^*$. As the impact velocity $v_i$ increases to 12 km/s, the plastic deformation of CNT films implemented by sliding and bending of the CNT fibers is hugely restricted due to the high loading rate. $\Delta E_s/\Delta E_b$ always increases initially above 1 and then decreases constantly no matter how many crosslinks are added, indicating a stable stretching-bending two-stage energy dissipation mode. As not much difference was observed for other crosslink densities, only the results for $\rho$ = 0 and 20 under $v_i$ = 12 km/s are displayed in Fig. 6. This impact-velocity-dependent dissipation mode is not only of significance to reveal the process of energy dissipation of CNT films, but also important for optimizing the design of protective materials with network structure at different impact conditions.

The evolutions of microstructure morphologies of the CNT films with $\rho$ = 0, 10, and 20 as shown in Fig. 7 are carefully investigated at different scales to reveal the failure mechanism. At the small scale as shown in Fig. 7(a), the CNT fibers in the system bend severely for

$\rho$ = 0 and separate from others after impact due to the cascaded interface sliding compared to its original state. However, the CNT fibers with $\rho$ = 10 and 20 are still bonded together and bend slightly after impact. At the medium scale as given in Fig. 7(b), a bundle of molecules is selected and color-coded according to the local virial stress along the impact direction. The microstructure morphologies, as well as the local atom stress in both original state and after impact, are given for comparison. For all three crosslink densities $\rho$ = 0, 10, and 20, the molecules on the edge of the conic deformation region beneath the projectile experience a transition from the relatively relaxed state with near-zero stress distribution to a hybrid state with most tensile and some compressive stress induced by impact. Fig. 7(a) and (b) show that both bending and stretching of fibers exist in such a network structure under impact regardless of the impact velocity and crosslink density. With the increase of crosslink density, the bending effect is relatively restricted, whereas the stretching effect dominates the deformation and provides more channels to dissipate energy. At the large scale as shown in Fig. 7(c), perforated holes are eventually formed due to the continuous breaking of covalent bonds as marked by the red beads. The size of the penetration hole decreases with increasing the crosslinks' density. In addition, the large-deformation regions near the periphery of the perforated holes also appear.

### 3.5. Effects of length, bending stiffness, and thickness of CNT film

Three key factors, length and bending stiffness of constituent CNTs, and thickness of CNT film were investigated to illuminate their effects on the ballistic resistance of CNT films. Fig. 8(a) shows the relationship between the specific penetration energy $E_p^*$ and the dimensionless length $\eta = L/D$ at $v_i$ = 8 km/s, where $L$ and $D$ are the length of CNTs and the projectile diameter, respectively. $E_p^*$ is barely dependent on the length of constituent CNT fibers for $\rho$ = 0 and 10
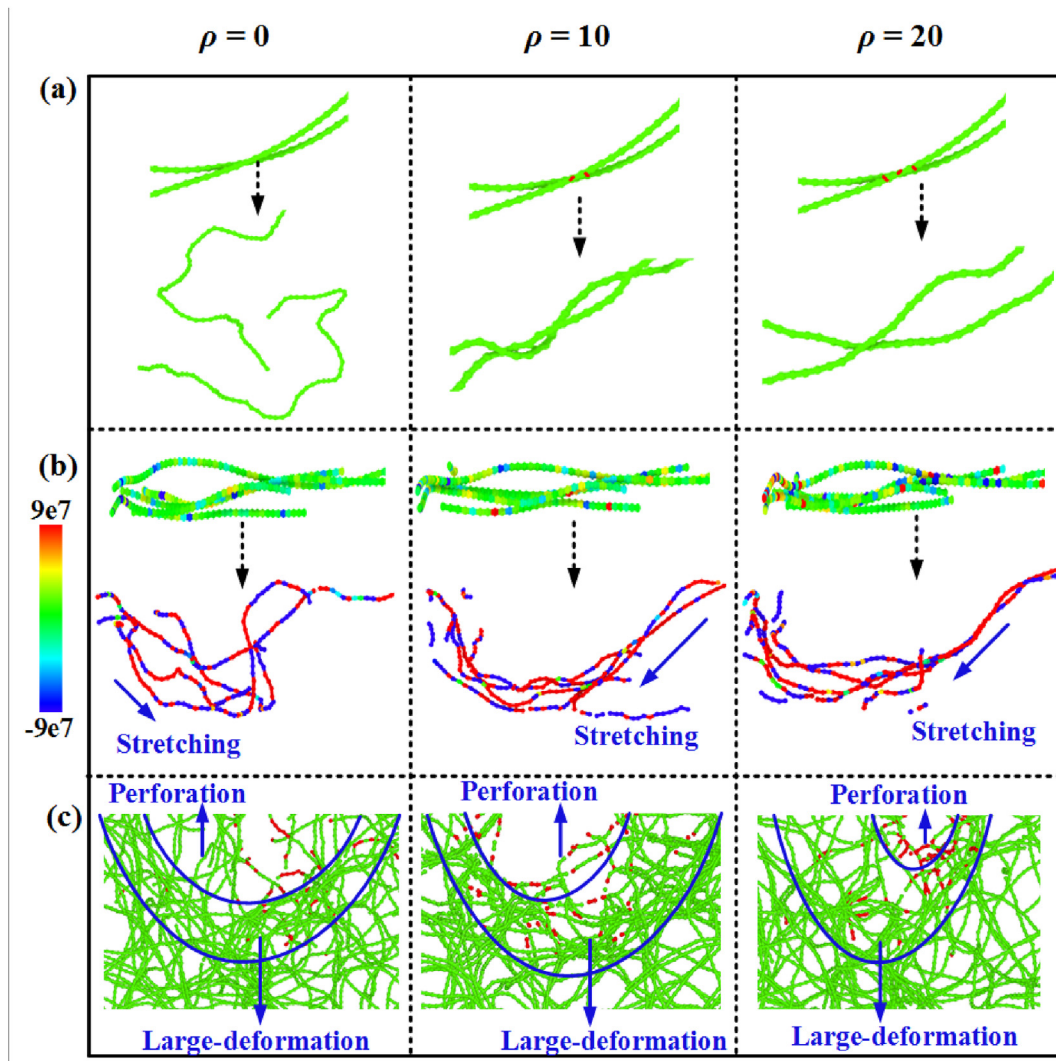
**Fig. 7.** Evolution of microstructure morphologies of CNT films from simulations with $\rho = 0$, 10, and 20 at (a) small scale showing the bending degree decrease with $\rho$, (b) medium scale indicating the hybrid state with most tensile and some compressive stress, and (c) large scale demonstrating the formation of penetration hole and large-deformation region, respectively. The marked red beads in (c) represent the broken bonds. (A colour version of this figure can be viewed online.)
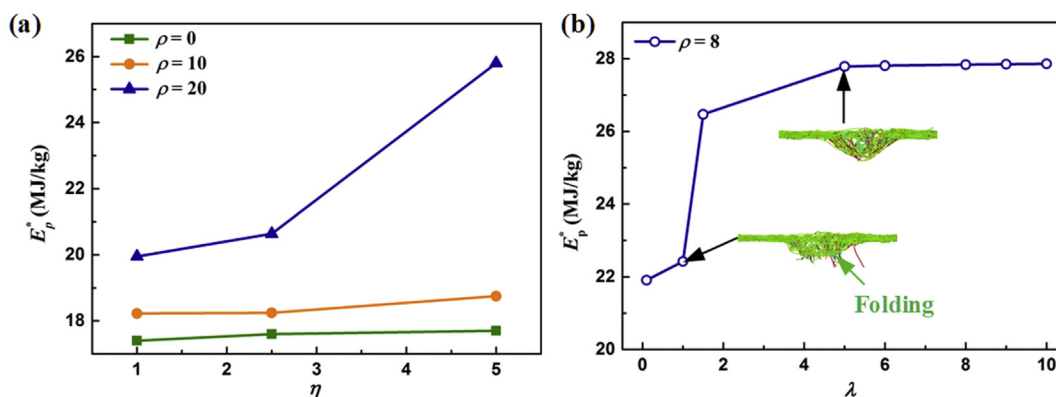


**Fig. 8.** Dependence relationship of the simulated specific penetration energy $E_p^*$ on (a) the ratio $\eta$ for the films with various $\rho = 0$, 10, and 20; and (b) the bending stiffness $\lambda$ for the film with $\rho = 8$. (A colour version of this figure can be viewed online.)

because the energy dissipation is mainly implemented by the intertube sliding for low crosslink densities. This is consistent with the previous finding that the energy dissipation efficiency of CNT films

without crosslinks varies scarcely with the length of the CNTs [19]. However, $E_p^*$ increases drastically with respect to $\eta$ for $\rho = 20$, indicating that the energy dissipation capability can be effectively

enhanced by increasing the length of CNTs only if enough crosslinks are introduced to generate more inter-tubes bridges and restrain the inter-tubes sliding.

To understand the effects of bending stiffness, a series of bending stiffness was studied by altering the $k_\varphi$ in Table 1 with a factor $\lambda$ from 0.1 to 10 [30,35] at $\rho = 8$ and $v_i = 6$ km/s to reflect the CNT films from perforation to non-perforation with the increase of bending stiffness. As shown in Fig. 8(b), $E_p^*$ increases quickly with respect to $\lambda$ for $\lambda \leq 1.5$, and then it increases slowly with the increase of $\lambda$ for $1.5 < \lambda \leq 5$. For $\lambda > 5$, $E_p^*$ is saturated, implying that there is a critical bending stiffness $k_{\varphi c}$, corresponding to $\lambda = 5$, for the present CNT film system. The insets of Fig. 8(b) show the hanging CNT chains around the edge of the perforated hole exhibit folding characteristics for $\lambda = 1$, and the CNT essentially becomes more rigid with the increment of bending stiffness with increasing $\lambda$ (e.g. for $\lambda = 5$). This result is consistent with the study by Mylvaganam et al. [19], which demonstrates that the single CNT with larger radii, i.e. larger stiffness, own more capability to resist faster bullet impact through full-atom MD simulations. It is to be noted this critical bending stiffness is dependent on the crosslink density, length of CNT fibers, and impact velocity based on the above results. The coupling effects of these parameters on the protective performance will be performed in the future to guide the optimization of the CNT films.

Besides, the thickness of the film is a crucial issue that affects the ballistic resistance of film materials. To investigate the effect of thickness, two relatively thick (i.e. $t = 10$ nm and 15 nm) CNT films for crosslinks' density $\rho = 10$ at $v_i = 12$ km/s were also investigated as given in Fig. 9. Fig. 9(a) shows that the 5-nm-thick CNT film is fully perforated and exhibits apparent out-of-plane displacement. With the increase of thickness (see Fig. 9(b) and (c)), the impact energy is not adequate to perforate the CNT film and the projectile

bounces back after impact. The morphologies of the CNT films with thicknesses of 10 and 15 nm do not show noticeable change after the impact, implying the nominal elastic deformation of the CNT films. The change of the potential energy, $\Delta E$, as shown in Fig. 10(a), can be decomposed into the changes of bending energy, $\Delta E_b$, stretching energy, $\Delta E_s$, and vdW energy, $\Delta E_v$. From Fig. 10(a) and (b), it clearly show that the change of vdW interface energy is negligible, and stretching and bending of the CNT chains are the dominant energy dissipation methods for all the thicknesses. Fig. 10(c) shows the ratio of the number of broken bonds to the total bond number in the system, $n$, to characterize the damage degree of the CNT film. The $n$ decreases quickly from 5.80‰ to 0.23‰ with increasing the thickness from 5 nm to 10 nm. Then it keeps almost at the same level with continually increasing the thickness to 15 nm. As shown in Fig. 10(d), $E_p^*$ increases with respect to thickness, $t$, of the CNT film, implying that more impact energy can be dissipated by the thick films. Three movies are provided in Supplementary materials to show the dynamical responses for three thicknesses with $\rho = 10$ at $v_i = 12$ km/s. Details are omitted here for simplicity.

According to the simulation results as shown in Figs. 9 and 10, there is not obvious transition of energy dissipation mode for the CNT films with increasing the thickness from 5 nm to 15 nm. However, for the thin CNT film with a thickness of 5 nm, the in-plane tension induced stretching and bending provide the mainly impact energy dissipation channels, whereas both the local compression and in-plane tension induced stretching and bending of CNT chains contribute to the impact energy dissipation for the relatively thick CNT films with thicknesses of 10 and 15 nm.

In addition to introducing more crosslinks, we have four methods to improve the impact resistance of CNT film based on the results in this paper: the first is to add crosslinks to enhance the
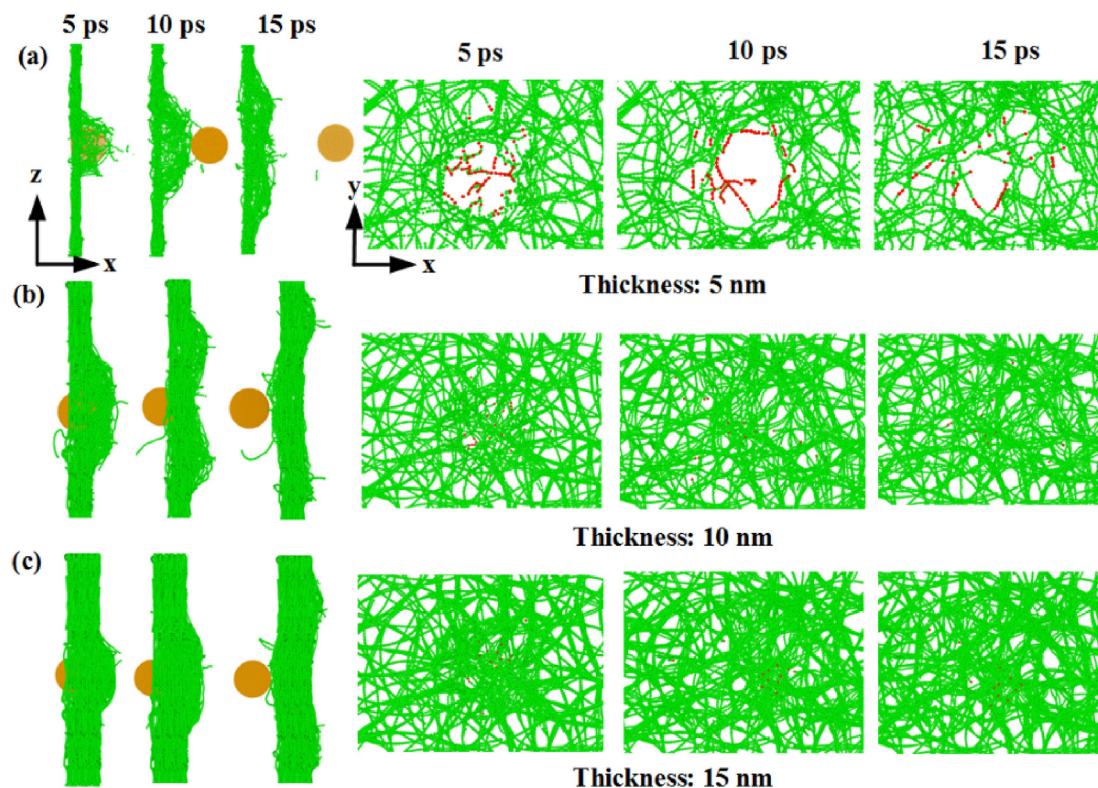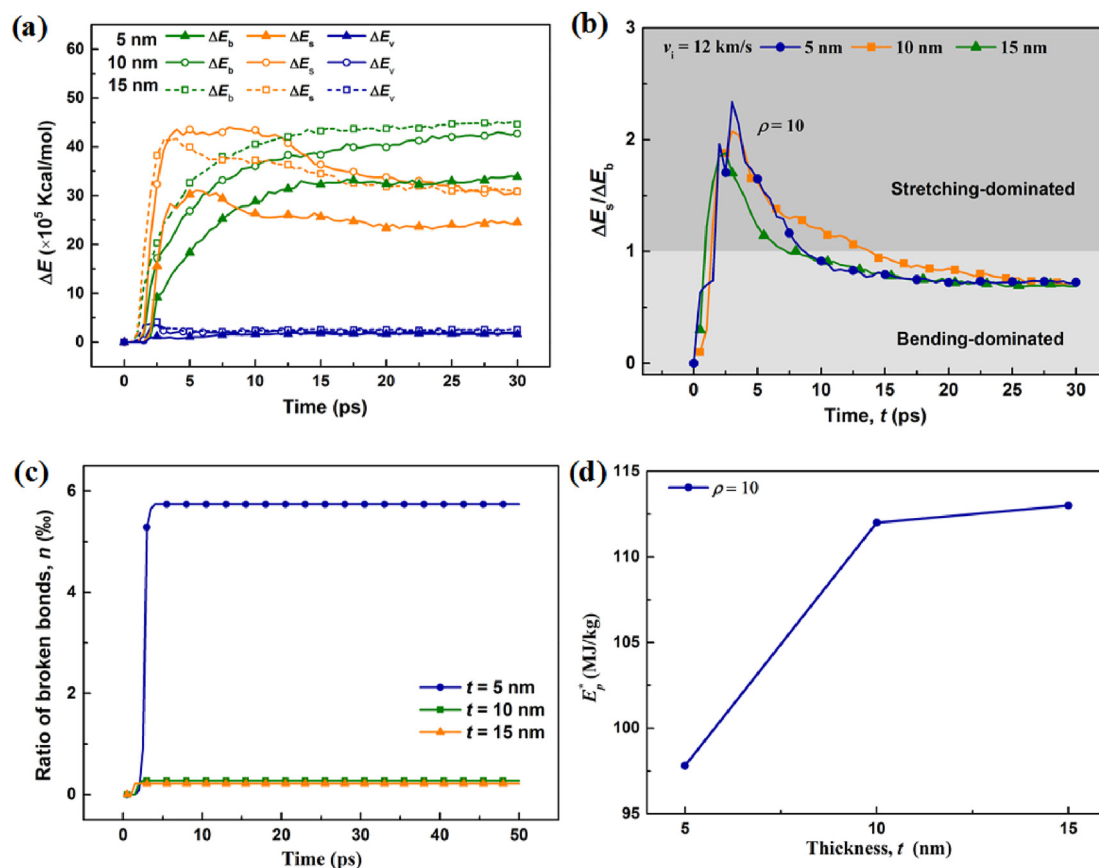


**Fig. 9.** Simulated morphologies of the CNT films with thicknesses of (a) 5 nm, (b) 10 nm, and (c) 15 nm for $\rho = 10$ during impact. (A colour version of this figure can be viewed online.)

**Fig. 10.** (a) Potential energy histories, (b) $\Delta E_s/\Delta E_b$, (c) ratio of broken bonds, and (d) specific penetration energy, $E_p^*$, of the CNT films with various thicknesses based on the CGMD simulations. (A colour version of this figure can be viewed online.)

inter-tube connections; the second is to increase the bending stiffness of CNTs, which can be realized by employing multiple walled carbon nanotubes with larger diameter; the third is to utilize long CNTs, which has also been studied by Bai et al. [44]; the last one is to increase the thickness of CNT film with densification procedure, as the study by Gao et al. [45]. It is noted that the regulation schemes abovementioned should also be applicable to enhance the anti–penetration ability of other CNT assemblies like CNT aerogels [46—48].

## 4. Conclusions

The impact resistance of CNT films with and without crosslinks was investigated by micro-ballistic impact experiments and CGMD simulations. The CGMD simulations qualitatively reproduced two typical experimental phenomena: the first one is the broken morphology around the penetration hole of the CNT film changing from the "fluffy" state to the "smooth" state after adding the PVA; the second one is the shrinkage of the perforation hole after adding PVA. The main conclusions can be further summarized as follows.

1. The introduction of crosslinks can efficiently enhance the efficiency of the energy dissipation of CNT film due to the enhanced interaction between adjacent CNTs by adding covalent bonds.
2. A transition from a system where the energy dissipation is dominated by the bending of the CNTs, to one in which the stretching-bending-dominated, is observed with increased density of crosslinks, implying more energy dissipation

channels can be activated at a high impact velocity and a high crosslink density.
3. For the high crosslinks' density, both increase the length of individual CNT and increase the thickness of CNT film can effectively improve the energy dissipation capability.
4. The increase of bending stiffness of CNTs can effectively increase the impact resistance of CNTs. However, for a given crosslink density, a critical bending stiffness is observed for the saturation of the protective performance of CNT film.

## Methods

**Materials.** The continuous CNT films were achieved by densifying CNT aerogels with almost flawless and high-crystallinity CNTs (diameter and length within the range of 0.7—15 nm and 300—360 μm respectively). The high-crystallinity CNTs were fabricated by floating catalyst chemical vapor deposition (FCCVD) method and collected at the end of the corundum tube layer by layer. The thickness of the CNT films was controlled by the number of winding layers. In this work, 10-μm-thick film was obtained by 10 layers of CNT aerogels, in which the CNT bundles were stacked randomly to form nano-network structures. The volume fraction of PVA is ~6.8%, which is negligible compared to that of the CNT chains and can be considered as an enhancement of CNT film to serves as crosslinks. The basic morphologies and quality of the adopted CNT films are characterized by SEM, Transmission Electron Microscopy (TEM), and Raman spectroscopy, as shown in Fig. 11. Fig. 11(a) and (b) show the prepared CNT films without and with PVA as
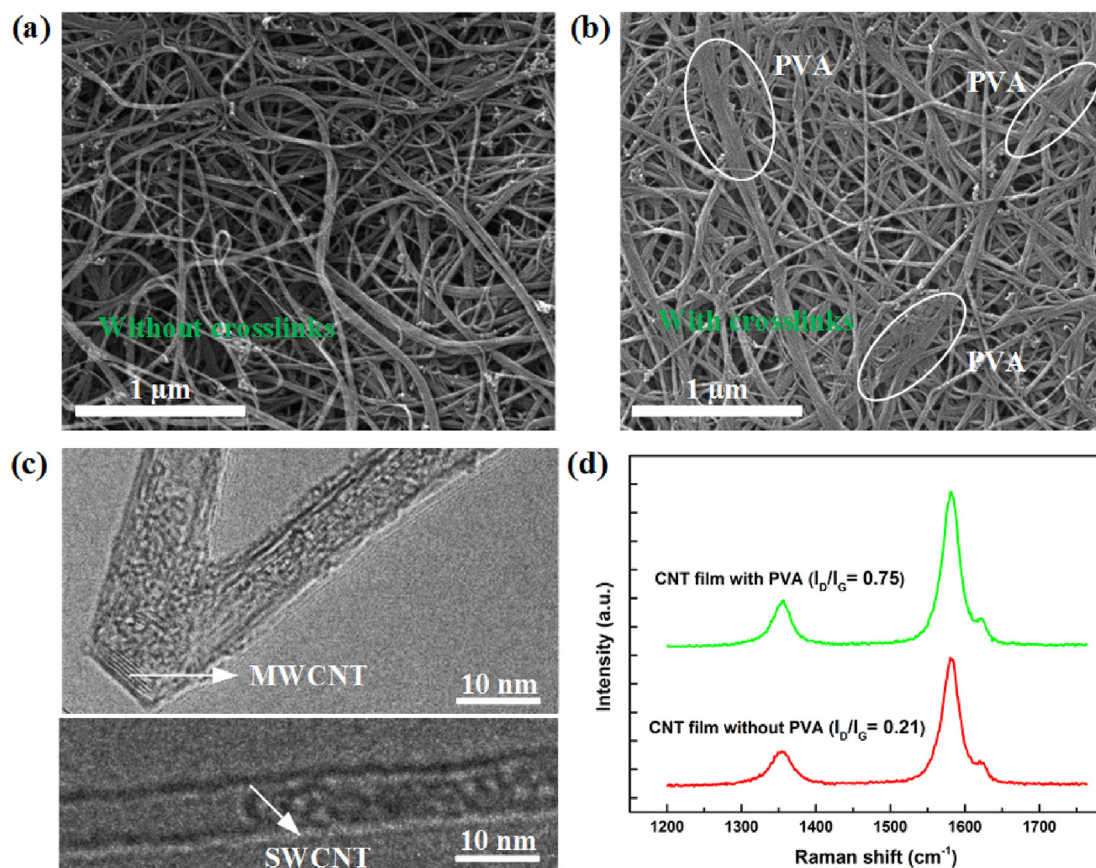
**Fig. 11.** The CNT film in (a) pristine state (i.e. without crosslinks) and (b) after adding PVA (i.e. with crosslinks), respectively, in which some obvious PVA enhanced regions have been marked by white circles). (c) TEM image illustrated the number of CNT walls. (d) Raman spectroscopy results indicated the quality of the CNT film. (A colour version of this figure can be viewed online.)

crosslinks, respectively, in which some obvious PVA enhanced regions have been marked by white circles in Fig. 11(b). After PVA was added, the binder effect will generate between CNT chains to enhance the weak vdW interfaces. The CNT in the experiments is a mixture of SWCNT and multi-wall CNT (MWCNT), and the diameter of the CNT ranges from 0.7 to 15 nm as shown in Fig. 11(c). Raman spectroscopy is employed to investigate the crystallization degree of the CNT film as shown in Fig. 11(d). The intensity ratio $I_D/I_G$ is used to characterize the structural integrity of the CNT film. For the CNT film without PVA, its crystallinity is relatively high. However, the nominal crystallinity of the CNT film decreases due to the appearance of the PVA.

**Fabrication of Numerical Sample.** The CNT film in the CGMD model is achieved by depositing 100 CNTs with initial curvatures on a rigid Lennard-Jones (LJ) wall placed at the bottom of the simulation box under body forces. The isothermal-isobaric ensemble (NPT) with Langevin thermostat at 300 K and Berendsen barostat at 0 Pa is applied during preparing the CNT film. The time step is set to be 10 fs. Once all the CNT chains reach almost equilibrium positions, the rigid wall and the body forces are removed, and the equilibrium-state pristine CNT film is obtained after a further 500,000 time-steps (i.e. 5 ns).

### CRediT authorship contribution statement

**Kailu Xiao:** Conceptualization, Methodology, Validation, Data curation, Formal analysis, Writing - original draft, preparation. **Xudong Lei:** Methodology, Investigation, Data curation. **Yuyu Chen:** Methodology, Investigation, Data curation. **Qi An:** Validation, Writing - review & editing. **Dongmei Hu:** Methodology, Validation, Data curation, Formal analysis. **Chao Wang:** Conceptualization, Validation, Methodology, Writing - review & editing. **Xianqian Wu:** Conceptualization, Methodology, Formal analysis, Writing - review & editing, Funding acquisition. **Chenguang Huang:** Supervision, Funding acquisition.

### Declaration of competing interest

The authors declare that they have no known competing financial interests or personal relationships that could have appeared to influence the work reported in this paper.

### Acknowledgments

### Appendix A. Supplementary data

Supplementary data to this article can be found online at https://doi.org/10.1016/j.carbon.2021.01.009.

# References

[1] S. Zangana, J. Epaarachchi, W. Ferdous, J. Leng, A novel hybridised composite sandwich core with Glass, Kevlar and Zylon fibres — investigation under low-velocity impact, Int. J. Impact Eng. 137 (2020) 103430.

[2] S. Khatiwada, C.A. Armada, E.V. Barrera, Hypervelocity impact experiments on epoxy/ultra-high molecular weight polyethylene fiber composites reinforced with single-walled carbon nanotubes, Procedia Eng 58 (2013) 4—10.

[3] S. Shrestha, B.D. Dunn, Plasma Electrolytic Oxidation and Anodising of Aluminium Alloys for Spacecraft Applications, Surface Engineering of Light Alloys, Woodhead Publishing, 2010, pp. 603—641.

[4] B.G. Cour-Palais, J.L. Crews, A multi-shock concept for spacecraft shielding, Int. J. Impact Eng. 10 (1) (1990) 135—146.

[5] M. Zhang, S. Fang, A.A. Zakhidov, S.B. Lee, A.E. Aliev, C.D. Williams, et al., Strong, transparent, multifunctional, carbon nanotube sheets, Science 309 (5738) (2005) 1215.

[6] J. Xu, Y. Li, Y. Xiang, X. Chen, A super energy mitigation nanostructure at high impact speed based on buckyball system, PloS One 8 (5) (2013) e64697-e64697.

[7] G. Lu, T. Yu, Energy Absorption of Structures and Materials, Woodhead Publishing, 2003, pp. 174—214.

[8] B. Xie, Y. Liu, Y. Ding, Q. Zheng, Z. Xu, Mechanics of carbon nanotube networks: microstructural evolution and optimal design, Soft Matter 7 (21) (2011), 10039-0.

[9] N. Anzar, R. Hasan, M. Tyagi, N. Yadav, J. Narang, Carbon nanotube - a review on Synthesis, Properties and plethora of applications in the field of biomedical science, Sensors Inter 1 (2020) 100003.

[10] S. Sakurai, F. Kamada, D.N. Futaba, M. Yumura, K. Hata, Influence of lengths of millimeter-scale single-walled carbon nanotube on electrical and mechanical properties of buckypaper, Nanoscale Res. Lett. 8 (1) (2013) 546.

[11] Y.J. Ma, X.F. Yao, Q.S. Zheng, Y.J. Yin, D.J. Jiang, G.H. Xu, et al., Carbon nanotube films change Poisson's ratios from negative to positive, Appl. Phys. Lett. 97 (6) (2010).

[12] S.W. Cranford, M.J. Buehler, In silicoassembly and nanomechanical characterization of carbon nanotube buckypaper, Nanotechnology 21 (26) (2010) 265706.

[13] W. Wang, Y. Zhang, L. Xu, X. Li, Mechanical properties of high-strength Q960 steel at elevated temperature, Fire Saf. J. 114 (2020) 103010.

[14] X. Liu, Z. He, J. Ye, L. Yan, S. Li, Y. Tang, Study on dynamic mechanical behavior of Q460JSC and HQ600 high strength steel, J. Constr. Steel Res. 173 (2020) 106232.

[15] J.J. Andrew, S.M. Srinivasan, A. Arockiarajan, H.N. Dhakal, Parameters influencing the impact response of fiber-reinforced polymer matrix composite materials: a critical review, Compos. Struct. 224 (2019) 111007.

[16] T.-L. Chu, C. Ha-Minh, A. Imad, A numerical investigation of the influence of yarn mechanical and physical properties on the ballistic impact behavior of a Kevlar KM2® woven fabric, Compos. B Eng. 95 (2016) 144—154.

[17] C. Wang, B. Xie, Y. Liu, Z. Xu, Mechanotunable microstructures of carbon nanotube networks, ACS Macro Lett. 1 (10) (2012) 1176—1179.

[18] S. Wang, E. Gao, Z. Xu, Interfacial failure boosts mechanical energy dissipation in carbon nanotube films under ballistic impact, Carbon 146 (2019) 139—146.

[19] H. Chen, L. Zhang, J. Chen, M. Becton, X. Wang, H. Nie, Energy dissipation capability and impact response of carbon nanotube buckypaper: a coarse-grained molecular dynamics study, Carbon 103 (2016) 242—254.

[20] A. Satti, A. Perret, J.E. Mccarthy, K. GkY, Covalent crosslinking of single-walled carbon nanotubes with poly(allylamine) to produce mechanically robust composites, J. Mater. Chem. 20 (37) (2010) 7941.

[21] S. Qu, X. Jiang, Q. Li, L. Gao, G. Zhou, D. Zhang, et al., Developing strong and tough carbon nanotube films by a proper dispersing strategy and enhanced interfacial interactions, Carbon 149 (2019) 117—124.

[22] S. Wang, Z. Liang, B. Wang, C. Zhang, High-strength and multifunctional macroscopic fabric of single-walled carbon nanotubes, Adv. Mater. 19 (9) (2007) 1257—1261.

[23] T. Filleter, R. Bernal, S. Li, H.D. Espinosa, Ultrahigh strength and stiffness in cross-linked hierarchical carbon nanotube bundles, Adv. Mater. 23 (25) (2011) 2855—2860.

[24] C. Wang, Y. Li, L. Tong, Q. Song, K. Li, J. Li, et al., The role of grafting force and surface wettability in interfacial enhancement of carbon nanotube/carbon fiber hierarchical composites, Carbon 69 (2014) 239—246.

[25] P. Lv, Y.Y. Feng, P. Zhang, H.M. Chen, N. Zhao, W. Feng, Increasing the interfacial strength in carbon fiber/epoxy composites by controlling the orientation and length of carbon nanotubes grown on the fibers, Carbon 49 (14) (2011) 4665—4673.

[26] C. Velasco-Santos, A.L. Martinez-Hernandez, V.M. Castano, Carbon nanotube-polymer nanocomposites: the role of interfaces, Compos. Interfac. 11 (8—9) (2005) 567—586.

[27] J.H. Lee, P.E. Loya, J. Lou, E.L. Thomas, Dynamic mechanical behavior of multilayer graphene via supersonic projectile penetration, Science 346 (6213) (2014) 1092—1096.

[28] M. Hassani-Gangaraj, D. Veysset, K.A. Nelson, C.A. Schuh, Melting can hinder impact-induced adhesion, Phys. Rev. Lett. 119 (17) (2017).

[29] M. Hassani-Gangaraj, D. Veysset, K.A. Nelson, C.A. Schuh, Melt-driven erosion in microparticle impact, Nat. Commun. 9 (1) (2018) 5077.

[30] S. Cranford, H. Yao, C. Ortiz, M.J. Buehler, A single degree of freedom 'lollipop' model for carbon nanotube bundle formation, J. Mech. Phys. Solid. 58 (3) (2010) 409—427.

[31] M.J. Buehler, Mesoscale modeling of mechanics of carbon nanotubes: self-assembly, self-folding, and fracture, J. Mater. Res. 21 (11) (2011) 2855—2869.

[32] Q.-M. Tan, Fundamental Principles of Dimensional Analysis, Dimensional Analysis, Springer Berlin Heidelberg, Berlin, Heidelberg, 2011, pp. 7—16.

[33] C. Wang, E. Gao, L. Wang, Z. Xu, Mechanics of network materials with responsive crosslinks, Compt. Rendus Mec. 342 (5) (2014) 264—272.

[34] C. Wang, S. Chen, Viscoelastic properties of randomly entangled carbon nanotube networks under cyclic tension loading, Comput. Mater. Sci. 119 (2016) 46—51.

[35] T. Yang, C. Wang, Z. Wu, Crosslink-tuned large-deformation behavior and fracture mode in buckypapers, Carbon 159 (2020) 412—421.

[36] S. Plimpton, Fast Parallel Algorithms for Short-Range Molecular Dynamics, Academic Press Professional, Inc., 1995.

[37] A. Stukowski, Visualization and analysis of atomistic simulation data with OVITO—the Open Visualization Tool, Model. Simul. Mater. Sc. 18 (1) (2009), 015012.

[38] N.K. Gupta, M.A. Iqbal, G.S. Sekhon, Experimental and numerical studies on the behavior of thin aluminum plates subjected to impact by blunt- and hemispherical-nosed projectiles, Int. J. Impact Eng. 32 (12) (2006) 1921—1944.

[39] J. Dean, C.S. Dunleavy, P.M. Brown, T.W. Clyne, Energy absorption during projectile perforation of thin steel plates and the kinetic energy of ejected fragments, Int. J. Impact Eng. 36 (10) (2009) 1250—1258.

[40] B.L. Lee, T.F. Walsh, S.T. Won, H.M. Patts, J.W. Song, A.H. Mayer, Penetration failure mechanisms of armor-grade fiber composites under impact, J. Compos. Mater. 35 (18) (2001) 1605—1633.

[41] L.H. Abbud, A.R.A. Talib, F. Mustapha, H. Tawfique, F.A. Najim, Behaviour of transparent material under high velocity impact, Inter, J. Mech. Mater. E 5 (1) (2010).

[42] S. Leigh Phoenix, P.K. Porwal, A new membrane model for the ballistic impact response and V50 performance of multi-ply fibrous systems, Int. J. Solid Struct. 40 (24) (2003) 6723—6765.

[43] G.A. Buxton, N. Clarke, Bending to stretching' transition in disordered networks, Phys. Rev. Lett. 98 (23) (2007) 238103.1—238103.4.

[44] Y. Bai, R. Zhang, X. Ye, Z. Zhu, H. Xie, B. Shen, et al., Carbon nanotube bundles with tensile strength over 80 GPa, Nat. Nanotechnol. 13 (7) (2018) 589—595.

[45] E. Gao, W. Lu, Z. Xu, Strength loss of carbon nanotube fibers explained in a three-level hierarchical model, Carbon 138 (2018) 134—142.

[46] M.A. Worsley, S.O. Kucheyev, J.H.S. Jr, A.V. Hamza, T.F. Baumann, Mechanically robust and electrically conductive carbon nanotube foams, Appl. Phys. Lett. 94 (7) (2009) 787.

[47] J. Liu, W. Gong, Y. Yao, Q. Li, J. Jiang, Y. Wang, et al., Strengthening carbon nanotube fibers with semi-crystallized polyvinyl alcohol and hot-stretching, Compos. Sci. Technol. 164 (2018) 290—295.

[48] D. Hu, W. Gong, J. Di, D. Li, R. Li, W. Lu, et al., Strong graphene-interlayered carbon nanotube films with high thermal conductivity, Carbon 118 (2017) 659—665.